Scientific Research Communications

Research Article

Sci. Res. Comm. (2024)
Volume 4, Issue 2
doi: 10.52460/src.2024.008

Heat and Mass Transfer Model of Horizontal Tubular Absorbers for LiBr/H2O Absorption Refrigeration

Nuri Kayansayan[1,*] Sercan Acarer[2]

[1] Dokuz Eylül University (retired), Faculty of Engineering, Department of Mechanical Engineering, İzmir
[2] İzmir Kâtip Çelebi University, Faculty of Engineering and Architecture, Department of Mechanical Engineering, İzmir
[*] Corresponding author: sercan.acarer@ikcu.edu.tr

Received: 11.02.2024 Accepted: 13.07.2024

Abstract

This study delves into the absorption efficiency of a horizontal absorber using a LiBr-H2O solution. We developed a computationally fast and accurate two-dimensional model, which we validated against experimental data. The analysis focuses on key operational parameters such as solution inlet temperature, mass flow rate, and cooling water inlet temperature, revealing their intricate interplay and impact on absorption performance. Our findings highlight the substantial influence of cooling water temperature, showing a significant boost in absorption efficiency as the cooling water temperature decreases. Additionally, we explore the effects of solution mass flow rate, uncovering the delicate balance between increased heat transfer resistance and initial absorption efficiency at near the impingement region. This comprehensive study provides valuable insights into the dynamics of absorption systems, offering pathways to optimize design and operational strategies for enhanced performance.

Keywords: LiBr-H2O solution; absorption refrigeration; heat and mass transfer, absorber

1. Introduction

Absorption cooling systems use heat as a driving force and are an alternative to conventional gas compression cooling systems. These systems, known for over a century, have gained popularity due to environmental concerns and rising conventional energy costs. They are especially competitive when a cheap heat source like geothermal or solar energy is available (Tsai and Perez-Blanco, 1998).

An absorption cooling cycle uses a working pair, consisting of a refrigerant and an absorbent. Common pairs are LiBr/water and ammonia/water. Ammonia is advantageous due to its lower evaporation temperature, while LiBr's nonvolatility and high vapor affinity offer better absorption performance. However, LiBr's limited solubility can cause crystallization at lower temperatures (Florides et al., 2003).

Absorption refrigerators produce compression effects by absorbing and desorbing refrigerants, rather than compressing gas. Vapors are absorbed at low pressure and desorbed at high pressure using a heat source. Performance can be enhanced through a double-effect absorption cycle, increasing system efficiency (Qu, 2008).

The major components of an absorption cycle are the evaporator, condenser, generator, absorber, and heat exchanger, along with solution and water pumps, and an air purge system. Figure 1 and Figure 2 present the schematic and pressure-temperature diagram of a single-stage absorption cycle, respectively.

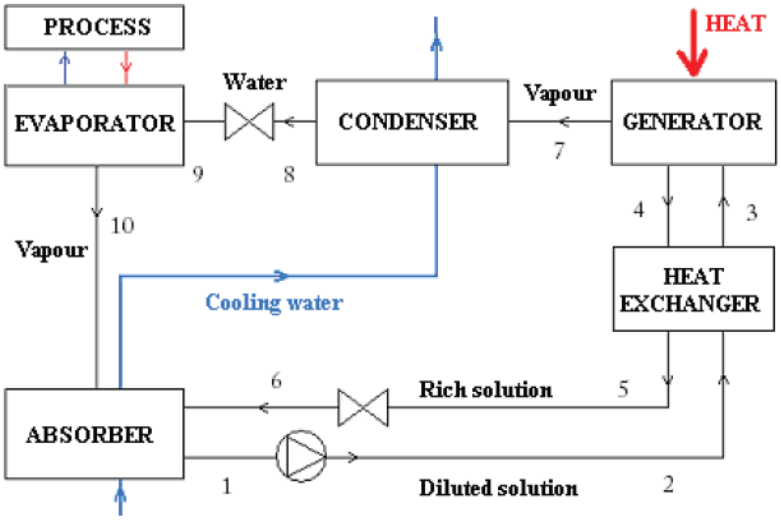

Figure 1. The schematic of a single-stage absorption cycle

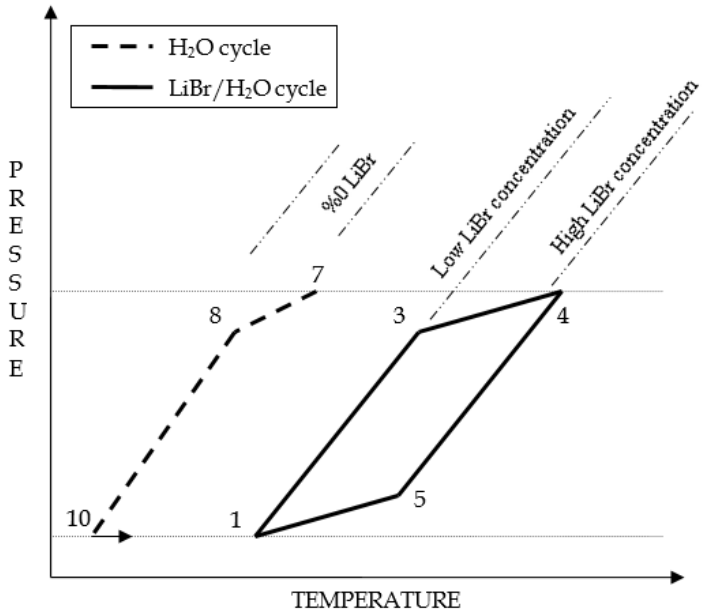

Figure 2. The pressure-temperature diagram of a single-stage absorption cycle

In the absorber, concentrated solution from the generator absorbs vapor, diluting the solution. Despite being central to the system, the absorber is often the least efficient component, making absorption rates a key performance measure (Raisul Islam et al., 2006).

Analytical studies have laid the groundwork for understanding the combined heat and mass transfer processes. Initial efforts, like those by Grigor'eva and Nakoryakov (1977), approached the problem by assuming a steady, smooth laminar film flow on an isothermal surface, simplifying the complex reality. Despite their comprehensive nature, these solutions demanded numerous assumptions, limiting their applicability.

As the limitations of analytical models became evident, particularly their reliance on oversimplified assumptions, the focus shifted towards numerical solutions. These models,

while rooted in the foundational principles laid out by their analytical counterparts, offer a more nuanced and flexible framework, capable of accommodating the irregularities and complexities inherent in real-world scenarios. Description of the problem will be introduced for absorption on a vertical plate, which is the simplest geometry for an absorber, where LiBr/H2O solution film flows down a vertical cooled plate while the refrigerant supplied from the evaporator is absorbed at the film surface (Figure 3).

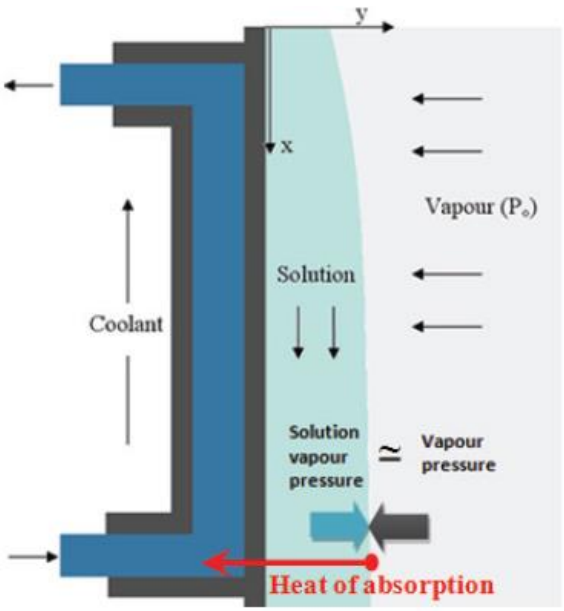

Figure 3. Absorber modeling problem shown on a simple vertical plate case

Andberg and Vliet (1983) and Andberg (1986) pioneered detailed numerical analysis by presenting a comprehensive numerical model, moving beyond the constraints of earlier analytical models. This evolution continued with subsequent studies, each progressively refining the model by integrating factors like film thickness variation, hydrodynamic characteristics, and more realistic boundary conditions.

Since then, many numerous studies have focused on heat and mass transfer modeling within absorbers (Wen et al., 2021; Asfand et al.,2015). These models often employ computational fluid dynamics (CFD) techniques to simulate the complex transport phenomena involved in the absorption process, including fluid mechanics of large droplets (Hosseinnia et al., 2016).

Empirical modeling techniques, known for their capacity to encompass transient behaviors and offer swift predictions for absorbers, have also become increasingly favored, as indicated by Castro et al. (2020). Optimization studies have aimed to improve the efficiency and performance of absorption cooling systems by varying parameters like absorber geometry, heat exchanger design and fluid properties (Sui et al., 2022a, Mortazavi et al., 2015). Numerical simulations coupled with optimization algorithms, such as genetic algorithms, have been employed to find optimal configurations (Sui et al., 2022b).

Numerical models are often validated against experimental data or higher order models to ensure their accuracy (Arroiabe et al., 2022). Researchers have presented case studies involving various absorber designs, operating conditions, and working fluid combinations (Asfand et al., 2016).

As numerical modeling tools continue to advance, the future of absorber modeling in absorption cooling systems may involve the incorporation of artificial intelligence and machine learning techniques for predictive modeling (Alcântara et al., 2023).

The present paper elaborates on the Lithium Bromide (LiBr) and water (H2O) solution which is dispersed from the top of the horizontal tubes, cascading down a vertically arranged set of tubes. Concurrently, vapor is continuously supplied from an evaporator under vacuum conditions. This flow format manifests as a falling film over the tubes and intermittently as unsteady droplets or elongated strands between tubes. The system is designed such that as the solution absorbs vapor, heat of absorption is generated. This heat must be dissipated into the surroundings via a cooling medium like water or air. Although there are more sophisticated models that include more intricate hydrodynamic models, this study focuses on creating a relatively straightforward and quick predictive model. This model is specifically designed for applications with low Reynolds numbers, where the surface waviness is minimal, and the tube is completely wetted.

2. Numerical Modeling

A solution of LiBr/H2O is dispersed over the top of the horizontal tubes, cascading down several vertically arranged horizontal tubes is considered. This occurs while a continuous stream of vapor from the evaporator is introduced under a vacuum. The liquid forms a descending film on the tubes, with intermittent droplets or extended trails bridging the tubes. The absorption of vapor by the solution triggers the production of absorption heat, which needs to be dispersed into the surrounding air or water.

In modeling the absorber, a two-dimensional slice of the film flow is segmented into distinct, non-overlapping Eulerian control volumes. The film's thickness changes along the flow direction, necessitating the creation of a body-fitted mesh (Figure 4).

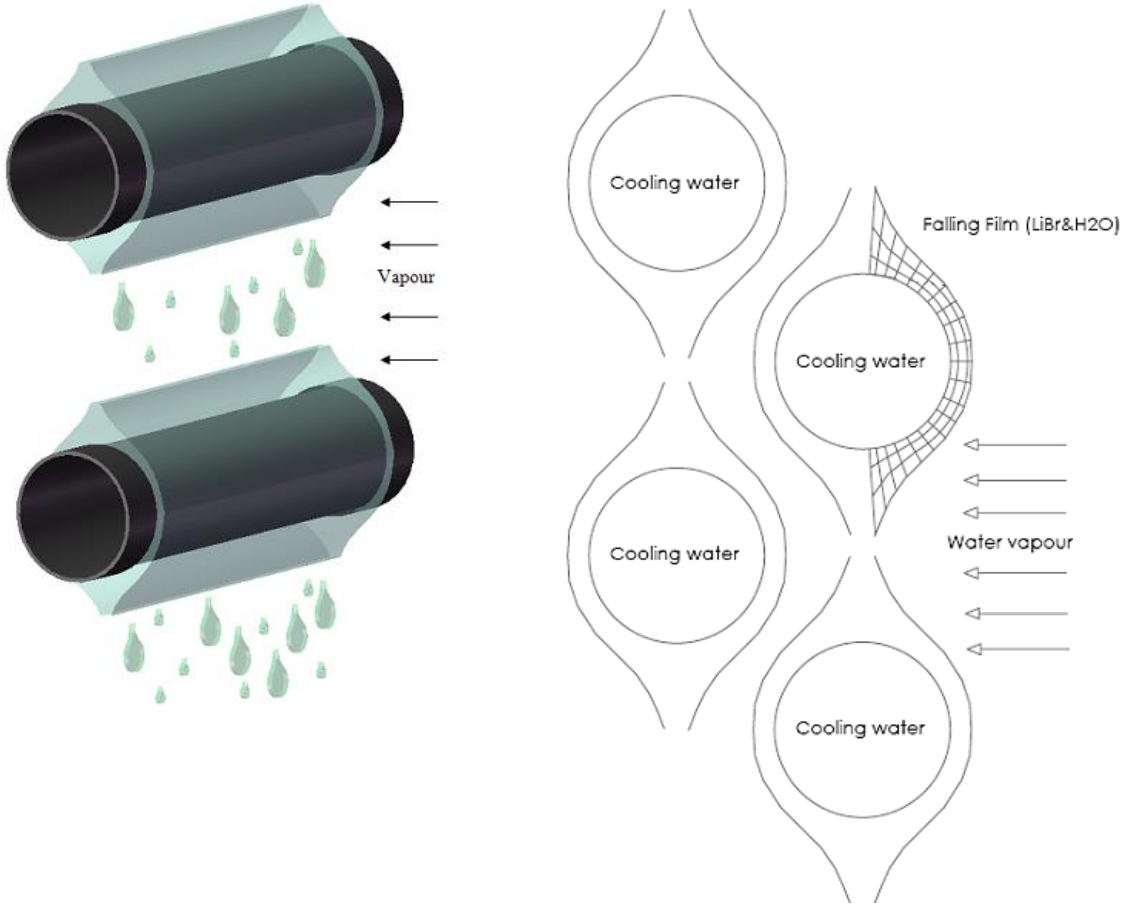

Figure 4. Horizontal absorber modeling

A coordinate transformation reconfigures the physical domain into a rectangular shape to streamline programming. The basic definition for the coordinate system and velocity components is shown in Figure 5.

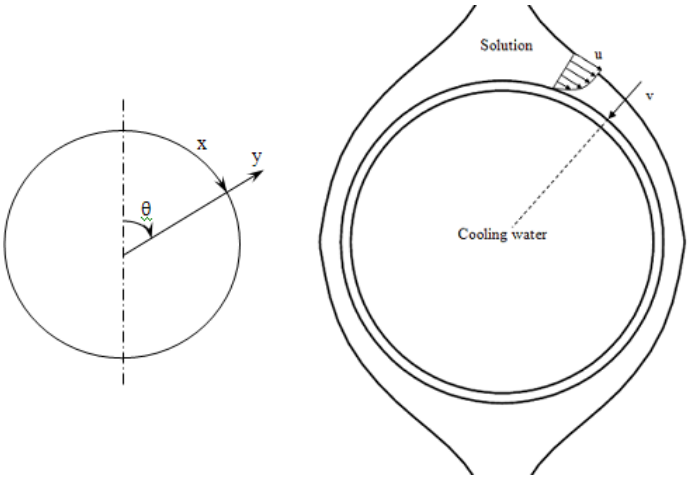

Figure 5. The coordinate system and velocity definitions

The model's characteristics include:

- Local variations in physical properties with temperature and concentration, though these variations are disregarded within each differential control volume.
- An increase in mass flow rate due to vapor absorption into the liquid film, leading to a change in film thickness across successive tubes.

The modeling is based on the following assumptions:

- The solution uniformly coats the tube.
- A balance in vapor pressure is maintained at the interface between the vapor and the solution.
- The flow is consistently laminar and smooth.
- Heat transfer is primarily in the solution, not the vapor phase, meaning all interface-generated heat is absorbed by the solution.
- The vapor exerts no shear stress on the film flow.
- Diffusion along the flow direction is considered insignificant.

The velocity profile of the film can be determined using the Navier-Stokes Equations. Given that the film's thickness is significantly smaller than the radius of the tube, it's practical to apply a Cartesian coordinate system for the film flow. In this scenario, viscous forces are the primary concern, allowing the neglect of inertial forces. It's also presumed that the pressure within the film remains uniform and that gravity serves as the primary force driving the flow.

Under these conditions, the steady-state Navier-Stokes Equation, oriented along the flow direction (as indicated by the x-axis in Figure 5), simplifies considerably:

$$\mu_s \frac{\partial^2 u}{\partial y^2} = -\rho_s g \sin\theta \tag{1}$$

Operating under the assumption that the vapor imparts no shear stress on the film, the velocity profile along the flow direction (represented by 'u' in Figure 5) can be deduced as follows:

$$u(x,y) = \frac{\rho_s g \delta^2}{2\mu_s} \sin\theta \left(2\frac{y}{\delta} - \left(\frac{y}{\delta}\right)^2 \right) \tag{2}$$

The velocity profile across the transverse direction (represented by 'v' in Figure 5) can be established based on the principle of continuity:

$$v(x,y) = -\frac{\rho_s g}{2\mu_s} y^2 \left[\frac{d\delta}{dx} \sin\theta + \frac{1}{r_o}\left(\delta - \frac{y}{3}\right)\cos\theta \right] \tag{3}$$

Local film thickness can be derived from u-velocity for a known solution mass flow rate:

$$\delta(\theta) = \left(\frac{3\mu_s \Gamma_s}{\rho_s^2 g \sin\theta} \right)^{1/3} \tag{4}$$

Where Γ_s is the solution mass flow rate per length and side of tube ($\Gamma_s = \dot{m}_s / 2L$) and ρ_s denotes solution density.

The steady-state energy balance for a differential control volume can be articulated using Cartesian coordinates, given that the usual measurements of film thickness are quite minor relative to the tube's diameter:

$$\frac{\partial(uT)}{\partial x} + \frac{\partial(vT)}{\partial y} = \alpha_s \frac{\partial^2 T}{\partial y^2} \tag{5}$$

The steady-state species balance for a differential control volume can be articulated in a similar manner as:

$$\frac{\partial(uC)}{\partial x} + \frac{\partial(vC)}{\partial y} = D \frac{\partial^2 C}{\partial y^2} \tag{6}$$

The flow rate of the solution film is significantly less than the cooling water's flow rate. As a result, the heat capacity of the cooling water is much greater than the solution's heat capacity. The combination of this, and the relatively brief length of the tube, results in the cooling water experiencing a much smaller increase in temperature compared to the solution. It can be concluded from a previous investigation (Papaefthimiouet al. 2006) that the temperature increase of the cooling water is linear in the axial direction of the tube. Hence cooling water temperature can be calculated at the half length of each tube, and this will represent the mean cooling water temperature for the tube. Heat transfer coefficient in the cooling water side is calculated from $Nu_b = 0.023 Re_b^{0.8} Pr_b^{0.4} (\mu_b/\mu_w)^{0.262}$ correlation which is valid for incompressible turbulent flow flowing inside a pipe (Kakaç and Liu, 1998).

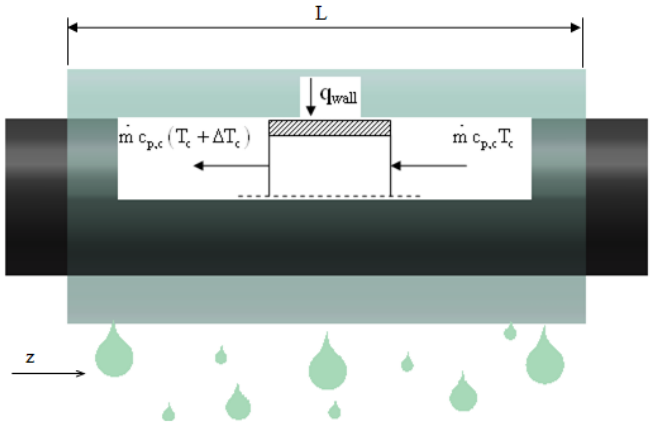

Figure 6. A one-dimensional differential control volume pertaining to the flow of cooling water within the tube

Cooling water temperature gradient expression for the cooling water can be derived from the one-dimensional energy balance shown in Figure 6 for the cooling arrangement presented in Figure 7:

$$\frac{dT_c}{dz} = \frac{(2\pi r_o)\, q_{wall-average}}{m_c\, c_{p,c}} \tag{7}$$

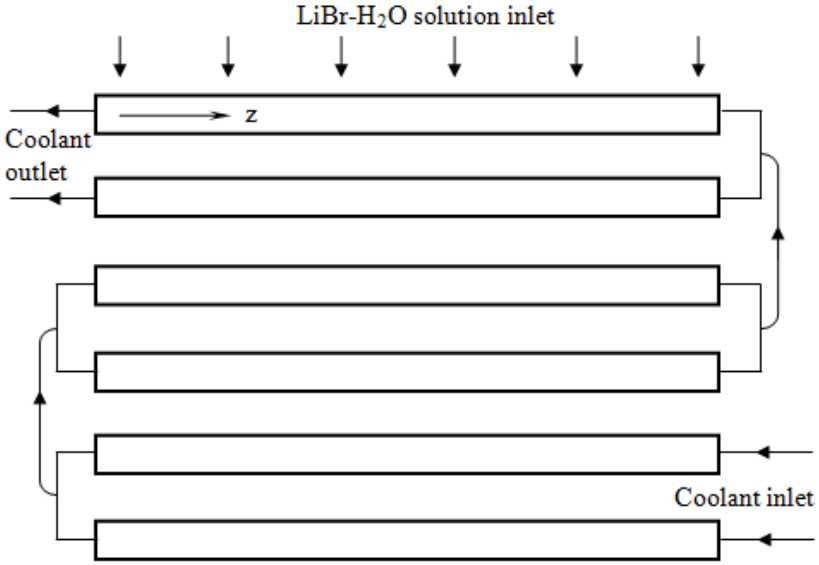

Figure 7. Tubes and the cooling water arrangement

Because the problem is a steady spatial marching problem, the calculation procedure must start from solution inlet, hence the boundary conditions at the inlet are categorized under "initial conditions". Initial conditions for the LiBr-H2O solution at the inlet (Figure 8) are:

$$\left.\begin{array}{l} x = x_{in} \\ 0 \le y \le \delta(x) \end{array}\right\} \quad \begin{array}{l} T = T_{in} \\ C = C_{in} \end{array} \tag{8}$$

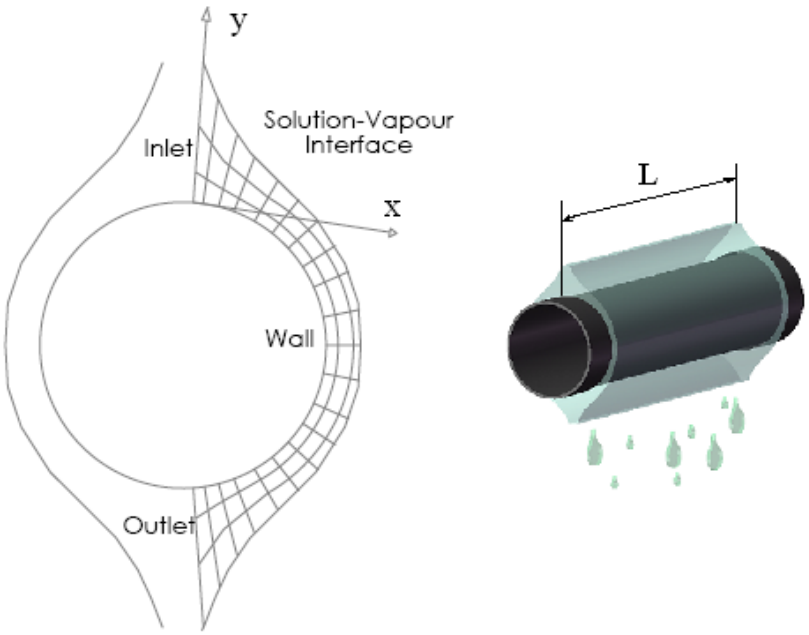

Figure 8. Edges of the physical area (left) and illustration of the tube's length (right)

The boundary conditions for the LiBr-H2O solution are as follows:

At the tube surface:

$$\left.\begin{array}{l} y = 0 \\ x_{in} \le x \le x_{out} \end{array}\right\} \quad \begin{array}{l} U\left(T - T_c\right) = k_s \dfrac{\partial T}{\partial y} \\ \dfrac{\partial C}{\partial y} = 0 \end{array} \tag{9}$$

U is the overall heat transfer coefficient calculated at the outer surface of the tube.

At the solution-vapour interface:

$$\left.\begin{array}{l} y=\delta(x) \\ x_{in} \le x \le x_{out} \end{array}\right\}$$

Mass flux is calculated from Fick's first law:

$$\dot{m}_{H_2O} = -\rho_s D \frac{1}{C_{if}} \frac{\partial C}{\partial y} \tag{10}$$

Vapour pressure equilibrium condition function is:

$$T_{if} = f(p, C_{if}) \tag{11}$$

Heat generation at the interface can be expressed as the product of mass absorption rate and heat of absorption per unit mass flow rate:

$$q_{if} = h_{abs} \dot{m}_{H_2O} \tag{12}$$

And heat of absorption is transferred into the solution:

$$q_{if} = -k_s \frac{\partial T}{\partial y} \tag{13}$$

At the exit, the temperature and concentration gradients along the flow direction are established as zero.

2.1. Coordinate Transformation

Because the film thickness changes with the circumferential (x) position (see Figure 5), a coordinate transformation process is needed in order to convert the complex domain into a non-dimensional square domain (see Figure 9), hence derivatives are normalized. This generally increases complexity of the governing equations, however simplifies the code considerably. Hence, we are considering the following non-dimensional variables:

$$X = \frac{\theta}{\pi} = \frac{x}{\pi r_o} \tag{14}$$

$$Y = \frac{y}{\delta(x)} \tag{15}$$

$$Z = \frac{z}{L} \tag{16}$$

Since Nusselt's solution results in an infinite film thickness at the top and bottom of the tube, the value of Y becomes unbounded at these extreme points. Therefore, to avoid this issue, areas near X=0 and X=1 are excluded from the domain of the solution.

By substituting Eqs. 14-16 into governing equations; Film thickness expression (Eq. 4) becomes:

$$\delta(\theta) = \left(\frac{3\mu_s \Gamma_s}{\rho_s{}^2 g \sin(\pi X)} \right)^{1/3} \tag{17}$$

Where Γ_s is the solution mass flow rate per length and side of tube ($\Gamma_s = \dot{m}_s / 2L$) and ρ_s denotes solution density.

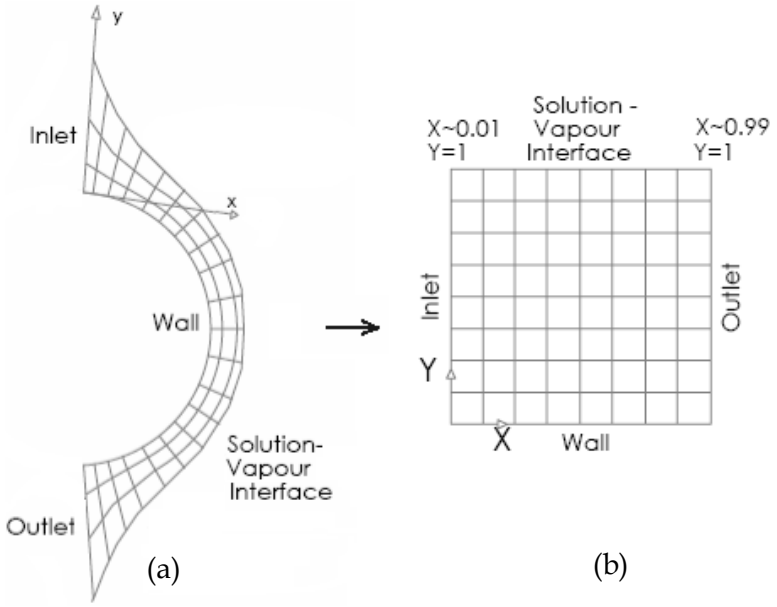

Figure 9. a) The area used for computation, b) The adjusted area designated for computation

The velocity profiles (Eqs.2,3) become:

$$u(X,Y) = \frac{\rho_s g \, \delta^2}{2\mu_s} \sin(\pi X)\left(2Y - Y^2\right) \tag{18}$$

$$v(X,Y) = -\frac{\rho_s g}{2\mu_s} Y^2 \; \delta^2 \frac{1}{r_o}\left[\frac{1}{\pi}\frac{d\delta}{dX}\sin(\pi X) + \delta\left(1 - \frac{Y}{3}\right)\cos(\pi X)\right] \tag{19}$$

The solution Reynolds, Prandtl and Schmidt numbers are defined as (respectively):

$$Re_s = \frac{4\Gamma_s}{\mu_s} \tag{20}$$

$$Pr_s = \frac{\mu_s c_{ps}}{k_s} \tag{21}$$

$$Sc_s = \frac{\mu_s}{\rho_s D} \tag{22}$$

Then, energy equation (Eq.5) becomes:

$$\frac{\partial T}{\partial X} - \left[\frac{v}{u}\frac{\pi r_o}{\delta} - \frac{Y}{\delta}\frac{d\delta}{dX}\right]\frac{\partial T}{\partial Y} - \left[\frac{8}{3}\frac{1}{Pr_s}\frac{\pi r_o}{\delta_{90}}\frac{\sin(\pi X)^{1/3}}{Re_s\left(2Y - Y^2\right)}\right]\frac{\partial^2 T}{\partial Y^2} = 0 \tag{23}$$

Species transport equation (Eq.6) becomes:

$$\frac{\partial C}{\partial X} - \left[\frac{v}{u}\frac{\pi r_o}{\delta} - \frac{Y}{\delta}\frac{d\delta}{dX}\right]\frac{\partial C}{\partial Y} - \left[\frac{8}{3}\frac{1}{Sc_s}\frac{\pi r_o}{\delta_{90}}\frac{\sin(\pi X)^{1/3}}{Re_s\left(2Y - Y^2\right)}\right]\frac{\partial^2 C}{\partial Y^2} = 0 \tag{24}$$

In Eq.23 and 24, δ_{90} is the film thickness at the middle of the tube (X=0.5).

The boundary conditions of the transformed governing equations (Equations 23 and 24) are deduced from the boundary conditions of the original governing equations in the following manner:

At the inlet (see Figure 9):

$$\left.\begin{array}{l} X = X_{in} \\ 0 \le Y \le 1 \end{array}\right\} \quad \begin{array}{l} T = T_{in} \\ C = C_{in} \end{array} \tag{25}$$

At the tube wall:

$$\left.\begin{array}{l} Y = 0 \\ X_{in} \le X \le X_{out} \end{array}\right\} \quad \begin{array}{l} T_{wall} = T_c + \left(\dfrac{k_s}{\delta_{mean} U}\right)\dfrac{\partial T}{\partial Y} \\ \dfrac{\partial C}{\partial Y} = 0 \end{array} \tag{26}$$

The term ‘ $k_s / (\delta_{mean} U)$ ’ is named as “CW”.

At the solution-vapor interface:

$$\left.\begin{array}{l} Y=1 \\ X_{in} \le X \le X_{out} \end{array}\right\}$$

Heat of absorption is transferred into the solution:

$$\frac{\partial T}{\partial Y} = -\frac{\rho_s D h_{abs}}{k_s}\frac{1}{C_{if}}\frac{\partial C}{\partial Y} \tag{27}$$

Vapor pressure equilibrium condition:

$$T_{if} = f(p, C_{if}) \tag{28}$$

At the outlet, gradients of temperature and concentration with respect to X are set to zero.

2.2. Deriving the Discretization Equations

The discretization equations are obtained using the control volume method. By assuming constant values of Y, δ(X), u, and v within a control volume, the transformed governing equations (Equations 23 and 24) are each integrated over a control volume:

$$\frac{\Delta Y}{\Delta X}\left(T_e - T_w\right) - \left[\frac{v}{u}\frac{\pi r_o}{\delta} - \frac{Y}{\delta}\frac{d\delta}{dX}\right]\left(T_n - T_s\right) - \left[\frac{8}{3}\frac{1}{Pr_s}\frac{\pi r_o}{\delta}\frac{\sin(\pi X)^{1/3}}{Re_s\left(2Y - Y^2\right)}\right]\left.\frac{\partial T}{\partial Y}\right|_s^n = 0 \tag{29}$$

$$\frac{\Delta Y}{\Delta X}\left(C_e - C_w\right) - \left[\frac{v}{u}\frac{\pi r_o}{\delta} - \frac{Y}{\delta}\frac{d\delta}{dX}\right]\left(C_n - C_s\right) - \left[\frac{8}{3}\frac{1}{Sc_s}\frac{\pi r_o}{\delta}\frac{\sin(\pi X)^{1/3}}{Re_s\left(2Y - Y^2\right)}\right]\left.\frac{\partial C}{\partial Y}\right|_s^n = 0 \tag{30}$$

Definitions of w, e, n, s, W, E, N and S points are illustrated in Figure 10.

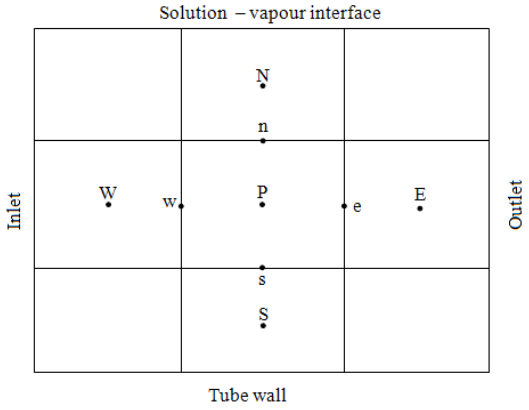

Figure 10. Illustrative diagram depicting the layout of the grid, along with explanations for the positions of the west, east, south, and north nodes, as well as the control surfaces

Cooling water energy balance becomes:

$$\frac{dT_c}{dZ} = -\left(\frac{\left(2\pi r_o\right)L\,k_s}{m_c\,c_{p,c}\delta_{mean}}\right)\left.\frac{\partial T}{\partial Y}\right|_{mean} \tag{31}$$

2.3. The Solution Method

In the transverse (y) direction, where the velocity is minimal and diffusion dominates, the upwind scheme is unsuitable, so the central differencing scheme is employed instead. In contrast, the downstream direction utilizes the upwind scheme (Patankar, 1980). The derivatives in Equations 29 and 30 for the inner nodes are calculated using the central difference formulation.

While the inlet temperature of the cooling water is known for the final tube in a counter-flow setup, the calculation begins with the first tube, necessitating an initial estimation of the outlet temperature of the cooling water. To accurately trace the decrease in cooling water temperature, it's crucial to solve a series of two-dimensional sections in sequence, adding a three-dimensional element to the solution. However, to manage the computational load, the

process is simplified by selecting only three axial positions, based on the premise of a linear reduction in cooling water temperature. Temperatures of the cooling water are recorded at the midpoint and end of each tube, respecting the counter-flow heat exchanger pattern where cooling water enters at the tube's end. The temperature at the tube's midpoint is taken as the average for that tube, while the temperature at the end is used as the exit temperature for the next tube in the sequence. A flowchart detailing the steps of this algorithm is shown in Figure 11.

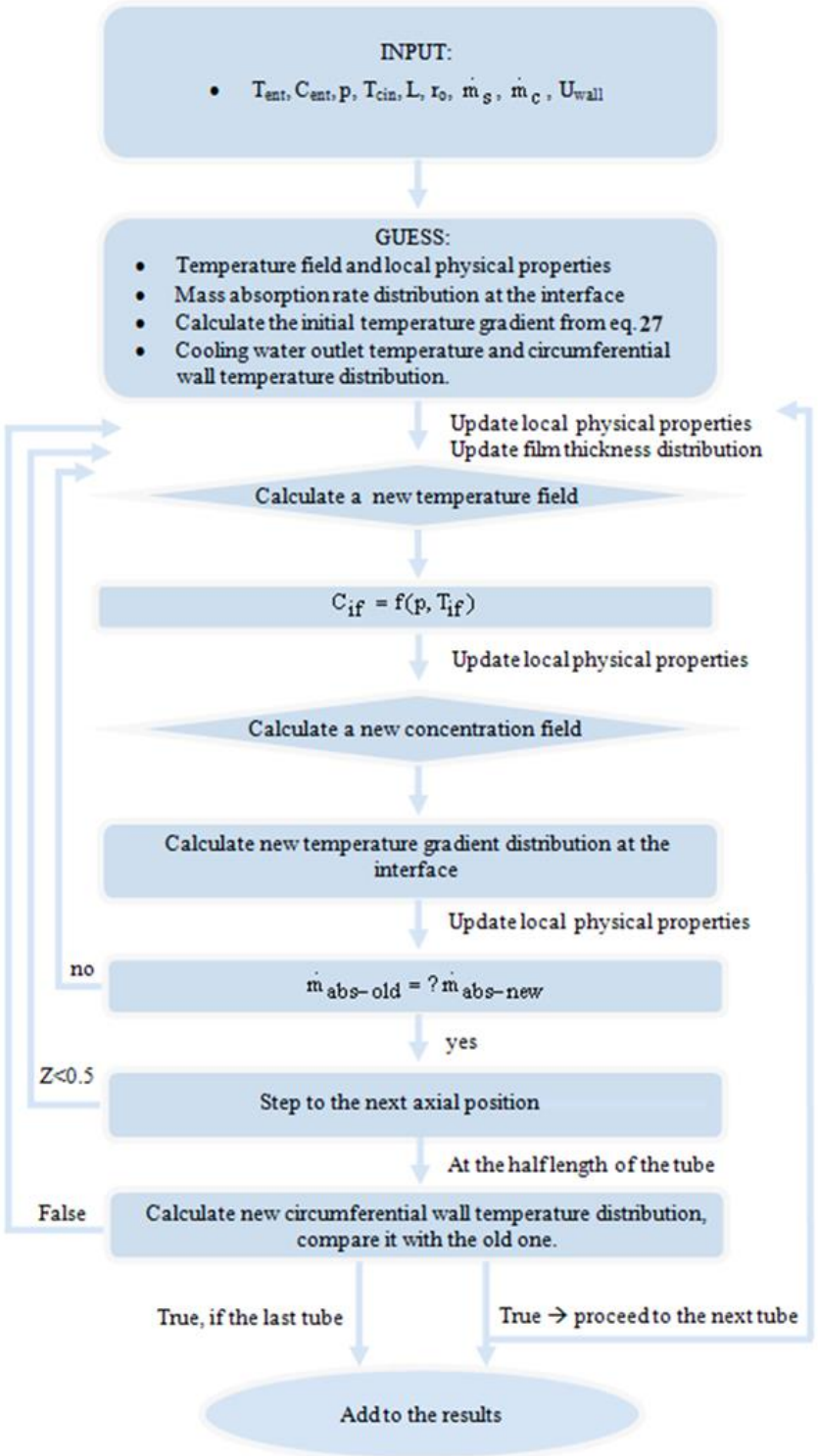

Figure 11. Diagram illustrating the sequence of steps in the algorithm for the horizontal absorber model

3. Results

This section outlines the findings obtained under various scenarios, including changes in vapor pressure, temperatures at the inlet and concentrations of the solution, cooling water's inlet temperature, mass flow rates, and the configuration of the tubes. These findings are compared with experimental data from prior studies to establish the limits of the current model's validity.

The distribution and average of vapor absorption flux are identified as the primary indicators of performance. Considering that the thickness of the film is affected by the film's Reynolds number and certain material characteristics, the patterns of mass (and thermal) flux are relevant to any system that matches the dimensionless figures inputted into the software.

The report includes charts showing how heat flux is distributed on the film's surface and along the wall. These factors are vital as mass transfer is closely associated with thermal transfer. Fundamentally, mass transfer can only proceed if the heat produced during absorption is efficiently transferred from the interface to the cooling water.

The physical properties of LiBr-H20 are compiled from multiple sources. Curve fits of experimental data for properties such as density, heat capacity, dynamic viscosity, and thermal conductivity are sourced from Kwang (1992):

$$\rho_s = 1000\,x\left(\left(0.7086 + 1.691\ x\ C\right) - 0.0005\ x\ T\right) \quad \left[kg/m^3\right] \tag{32}$$

$$c_{ps} = 1000\,x\,19.458\,x\,T^{0.05}\ x\ \left(100\ x\ C\right)^{-0.609} \quad \left[J/kgK\right] \tag{33}$$

$$k_s = 1.163\,x\left(0.4945 + 0.002052\ x\ T - 0.000015\ x\ T^2 - 0.31xC\right) \quad \left[W/m^2K\right] \tag{34}$$

$$\mu_s = \left(1 + 0.686602333\ x\ e^{\left(0.107\ x\ 100\ x\ C\right)}\ x\ T^{-1.238}\right) \Big/ 1000 \quad \left[Ns/m^2\right] \tag{35}$$

The curve fitting for the heat of absorption, originally formulated by Andberg (1986), has been revised to conform with the more accurate data presented by Papaefthimiou et al. (2006):

$$\begin{aligned} h_{abs} = {} & 2.5124\ x\ 10^6 - \left(283.3 + 1177\ x\ T\right) \\ & + 20152\ x\ (1660.47\ *\ C^7 - 2550\ x\,C^8 + 1410.1xC^9) \quad [J/kgK] \end{aligned} \tag{36}$$

The surface pressure equilibrium function ($C_{if} = f(p, T_{if})$), as sourced from Raisul Islam et al. (2006), is adopted and linearized:

$$C_{if} = \left(4.8688\ x\ 10^{-3}\ x\ p^{-0.188}\right) T_{if} + 0.37794 \tag{37}$$

Diffusivity is assumed to be constant:

$$D = 1.52\ x\ 10^{-9} \quad \left[m^2/s\right] \tag{38}$$

The local interfacial mass flux may be obtained by the expression:

$$\dot{m}(X) = \rho D\,\frac{1}{C}\,\frac{\partial C}{\delta(X)\,\partial X}\bigg|_{Y=1} \quad \left[kg/m^2s\right] \tag{39}$$

Where $\delta(X) = \left(0.75\ Re\ \upsilon_s^{\,2} / g / \sin(\pi X)\right)^{1/3}$ is the film thickness evaluated at the local bulk conditions at any circumferential position. It is important to note that it exclusively relies on

the local Reynolds number, temperature, and concentration (therefore, impacting the solution's viscosity and density). Consequently, the distribution of mass flux can be assessed for the partially nondimensional system, as previously mentioned.

Overall interfacial mass flux can be evaluated by directly averaging local mass fluxes:

$$\dot{m}_{mean} = \frac{\sum_{X_{in}}^{X_{out}} \dot{m}(X)}{n} \tag{40}$$

Where n is the number of cells in the downstream (x) direction.

Bulk temperature (T_b) and concentration (C_b) may be calculated as follows:

$$T_b = \frac{\sum_{\text{tube wall}}^{\text{film surface}} uT}{u_{mean}} \tag{41}$$

$$C_b = \frac{\sum_{\text{tube wall}}^{\text{film surface}} uC}{u_{mean}} \tag{42}$$

Where 'u' is the velocity component in the downstream direction.

3.1. Experimental Validation

The model's accuracy was validated using the experimental data from Seol and Lee (2005). As indicated in Figure 12, the model shows a good match for sheet flow drainage conditions.

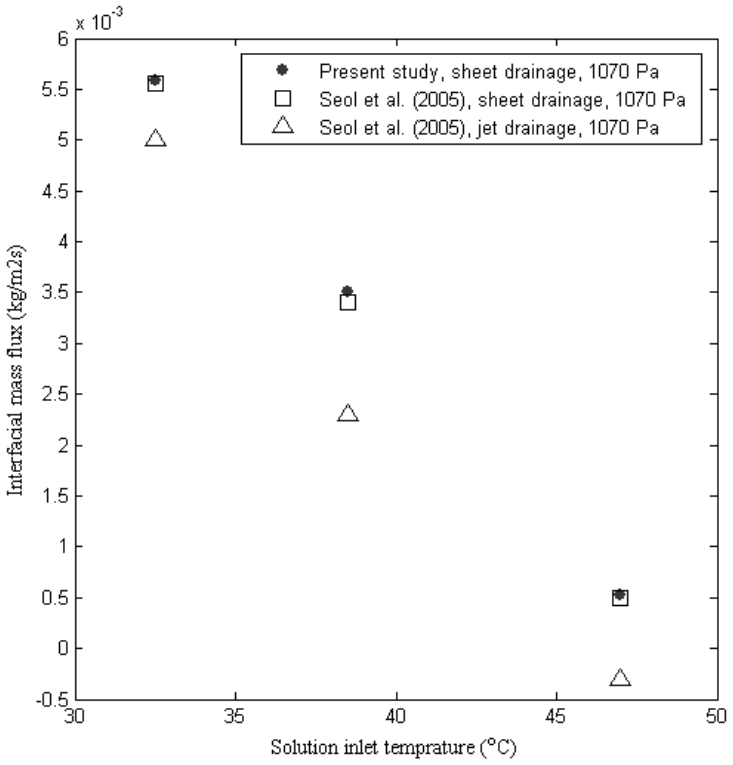

Figure 12. Variation of average mass flux with solution inlet temperature, comparing the present horizontal absorber model with experimental data of Seol and Lee (2005)

Typically, the solution drips in unsteady droplets or jets between tubes, but by placing a thin plate just beneath a tube, sheet drainage is deliberately formed. This arrangement ensures a uniform film flow on the tube surface, thereby enhancing performance at the specified mass flow rate. However, the current model falls short in predicting outcomes for jet drainage, as this form of drainage leads to time-dependent and unevenly distributed flow on the tube surface. Accurately modeling these effects would require a more complex, time-dependent, three-dimensional hydrodynamic model. Nonetheless, because performance improves with sheet drainage, the inability to model jet drainage is not always a significant drawback.

3.2. Parameter Space Being Investigated

The structural design of the horizontal absorber in question involves a solitary copper tube with external and internal diameters measuring 19.05 mm and 16.6 mm respectively, and a length of 0.5 m. The LiBr/H2O mixture is introduced at the top of the tube, flowing downward as a sheet. This sheet flow assumption is deemed realistic for the inner tubes (excluding the topmost tube) and can be achieved by installing a slim vertical plate just beneath the tube being tested, as suggested by Seol and Lee (2005). Typically, the solution cascades down in an irregular pattern of jet flows and droplets between the tubes.

A summary of the operational parameters is provided in Table 1, and the dimensionless inputs used in the developed code are detailed in Table 2.

Table 1. Physical parameters which satisfy the dimensionless inputs

	High solution inlet temperature		**Low solution inlet temperature**
T_{si}	46 °C		31 °C
C_{si}		0.6 (wt LiBr)	
m_{si}		0.00724 kg/s	
$\delta_{90i} = f(m_{si})$	0.15 mm		0.175 mm
p		1250 Pa	
r_o		9.525 mm	
r_i		8.3 mm	
L		0.5 m	
T_{ci}		30 °C	
m_c		0.43 kg/s	

Table 2. Program inputs at the inlet conditions

	High solution inlet temperature		**Low solution inlet temperature**
T_{si}	46 °C		31 °C
C_{si}		0.6 (wt LiBr)	
p		1250 Pa	
Re_s	6.186		4.137
Pr_s	21.13		32.146
Sc_s	1812.68		2699
$\Gamma r_o/\delta_{90i}$	195.415		171.38

3.3. Results for High Temperature Solution Inlet

Figure 13 and Figure 14 shows the temperature and concentration, respectively. The initial rise of temperature and subsequent cooling is evident from Figure 13. Figure 14 shows how vapor is absorbed and diffused and convected into the domain. Since the temperature profile is initially uniform (in the transverse direction) near the impingement point at the top (may be

called as the "inlet"), the absorption heat generated at the film's surface does not being transferred to the cooling water (See the flat profile in Figure 15), which restricts absorption efficiency. Yet, the tube wall is significantly cooler than the bulk of the solution, and the heat from absorption at the interface marginally raises the surface temperature. Consequently, just past the top impingement point (at X=0.002 and X=0.01), very high temperature gradients appear at the wall and film surface. The high temperature on the wall is responsible for rapid temperature drop at this position. On the interface, the high temperature gradient does not cause streamwise temperature drop since heat of absorption increases the surface temperature.

The corresponding concentration profile is shown in Figure 16. As the temperature profile evolves in the streamwise (X) direction, enabling heat transfer from the film's surface to the cooling water (Y direction), the absorption rate markedly increases. As vapor is absorbed in substantial amounts, the vapor concentration both at the surface and overall begins to rise, which reduces the absorption driving force (see Figure 14). The intense temperature gradients near the impingement point ("inlet" or "the top of the tube") result from substantial concentration gradients at the film surface (see X=0.002 and X=0.01), leading to extremely high absorption rates at the entrance (observe X<0.01). Consequently, the heat released from absorption prevents the drop of surface temperature. Near the impingement point, concentration gradients are high due to the elevated LiBr concentration near the surface, thus enhancing the absorption driving force.

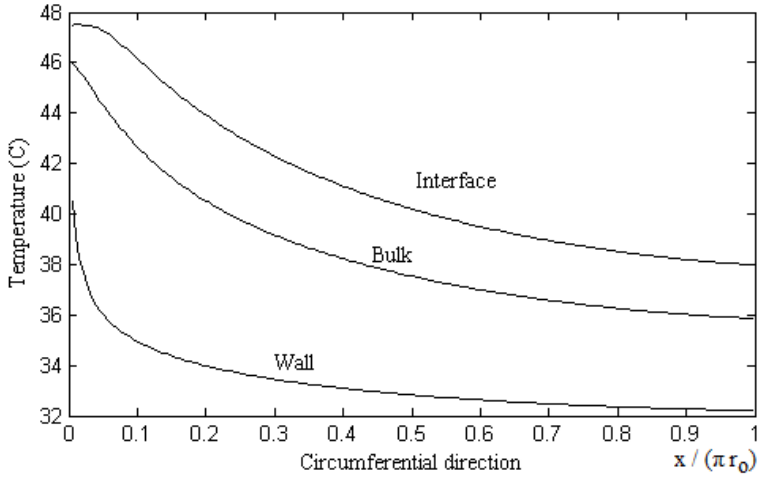

Figure 13. Variation of surface, wall and bulk temperature with distance around the tube, high temperature inlet (see Figure 9 for the definition of the domain)

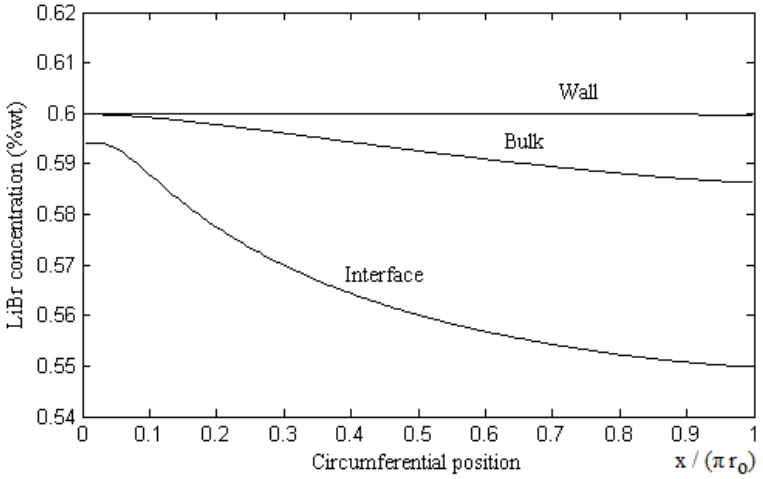

Figure 14. Variation of surface, wall and bulk LiBr concentration with distance around the tube, high temperature inlet (see Figure 9 for the definition of the domain)

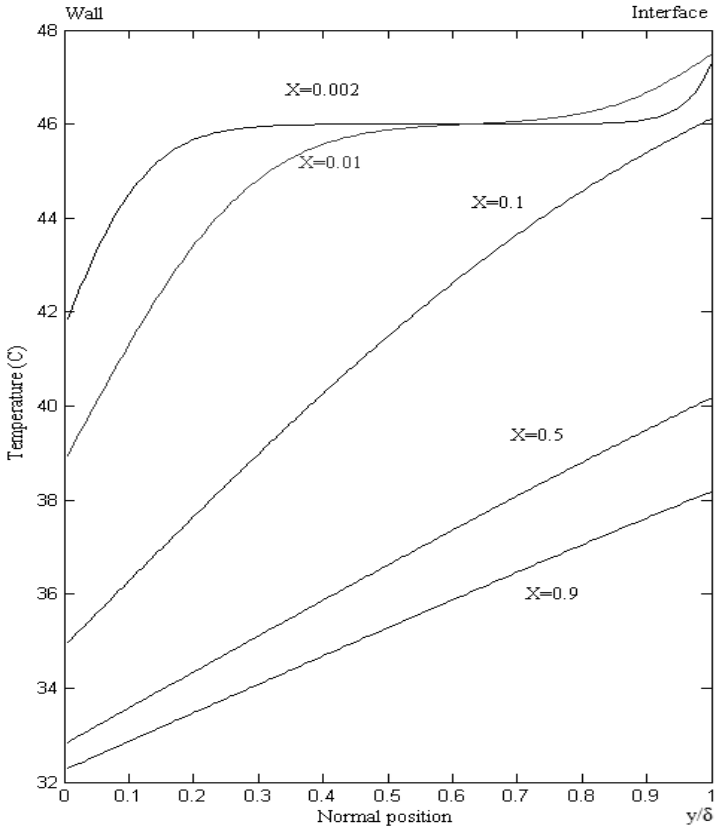

Figure 15. Cross stream temperature profiles at selected downstream positions, high temperature inlet (see Figure 9 for the definition of the domain)

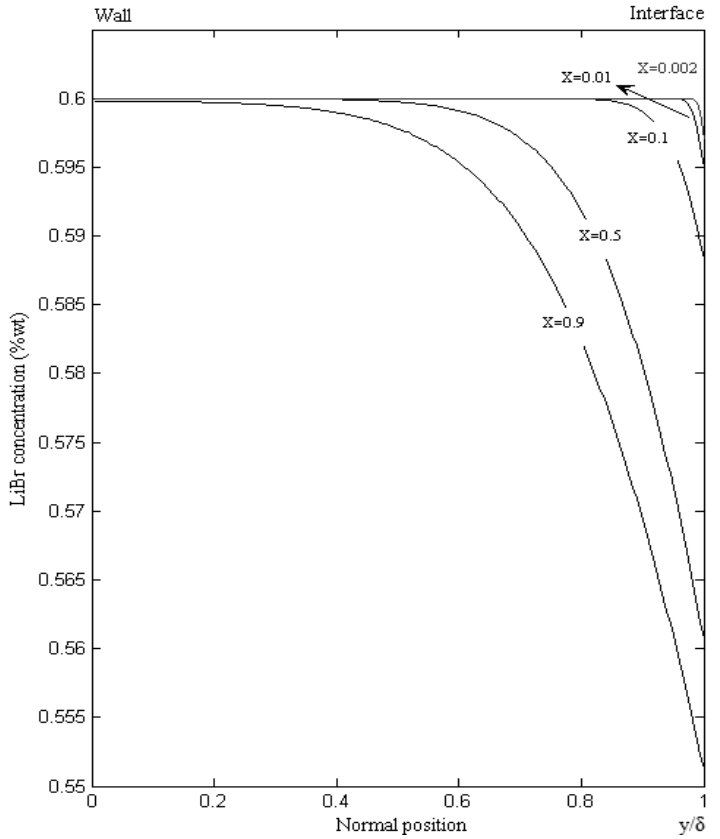

Figure 16. Cross stream LiBr concentration profiles at selected downstream positions, high temperature inlet (see Figure 9 for the definition of the domain)

Following the tube's 40% circumference (X>0.4, Figure 9) (refer to Figure 17), absorption rates begin to decrease gradually. This is mostly attributed to increased film thickness. Similarly, as the solution progresses towards the tube's end, the film thickens, which in turn heightens resistance to both heat and mass transfer (illustrated in Figure 18). Another reason is that since the vapor is absorbed in substantial amounts, the vapor concentration both at the surface and overall begins to rise, which reduces the absorption driving force (see Figure 14).

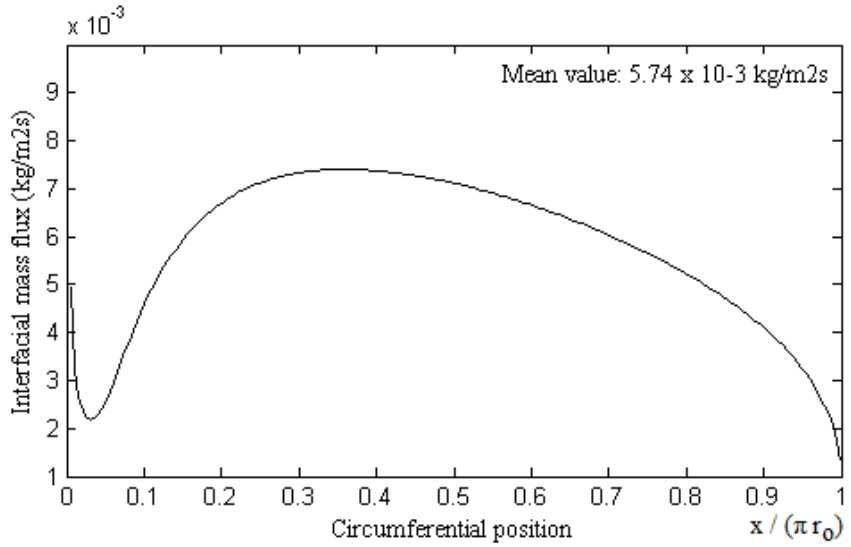

Figure 17. Variation of interface vapour absorption flux with distance around the tube, high temperature inlet (see Figure 9 for the definition of the domain)

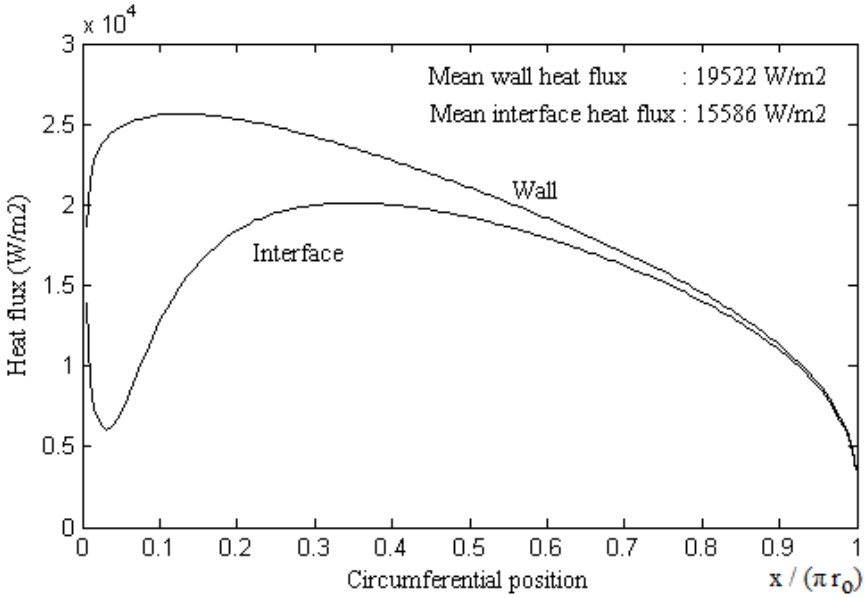

Figure 18. Variation of surface and wall heat flux with distance around the tube, high temperature inlet (see Figure 9 for the definition of the domain)

3.4. Results for Low Temperature Solution Inlet

Due to the notably low temperature at the inlet, there is a significant absorption activity aimed at equalizing the solution's vapor pressure with the absorber pressure. This leads to an increase in both bulk and surface temperatures, as depicted in Figure 19 until X~0.2 (see Figure 9 for the definitions). After that circumferential position, interface, bulk and wall temperatures gradually reduces as a result of increased cooling.

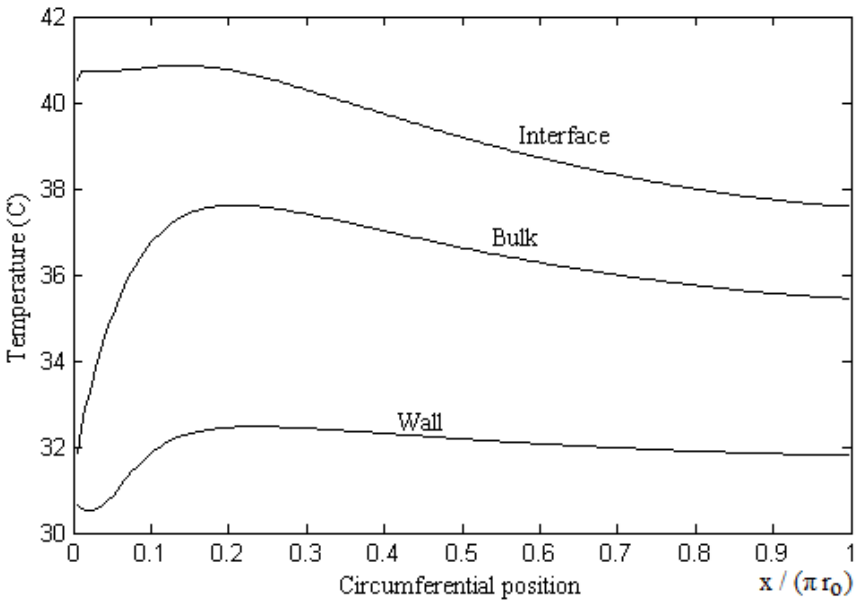

Figure 19. Variation of surface, wall and bulk temperature with distance around the tube, low temperature inlet (see Figure 9 for the definition of the domain)

However, since the temperature profile remains uniform in the transverse direction at the inlet, as shown in Figure 21, the absorption heat does not transfer to the cooling water. Figure 20 illustrates the variation of surface, wall, and bulk LiBr concentration with distance around the tube. In Figure 22, a more detailed presentation of this data in the transverse direction showcases the precise distribution of LiBr concentration, with convection and diffusion of the vapor smoothly captured.

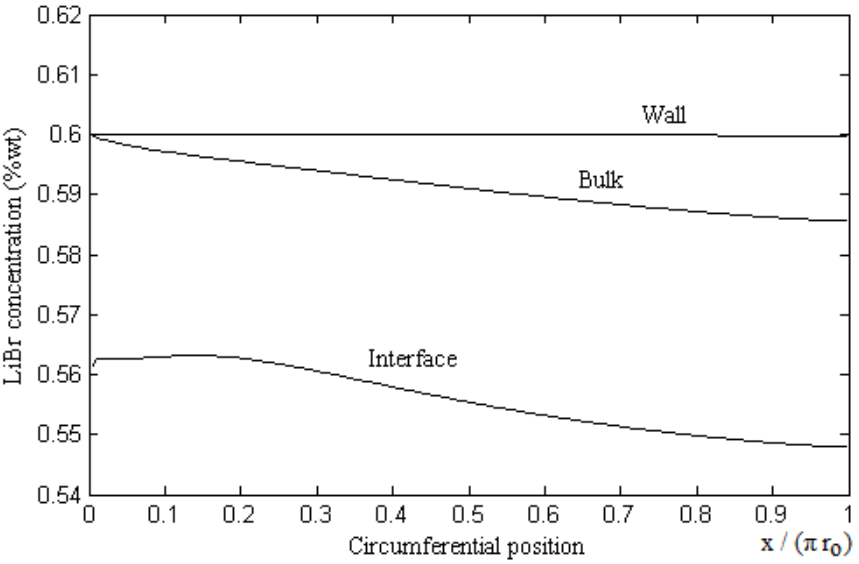

Figure 20. Variation of surface, wall and bulk LiBr concentration with distance around the tube, low temperature inlet (see Figure 9 for the definition of the domain)

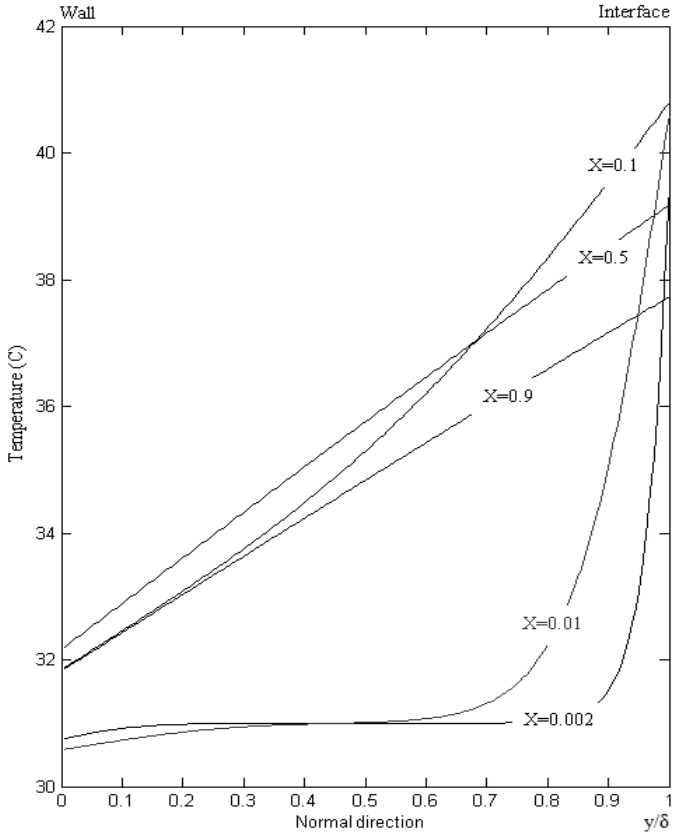

Figure 21. Cross stream temperature profiles at selected downstream positions, low temperature inlet (see Figure 9 for the definition of the domain)

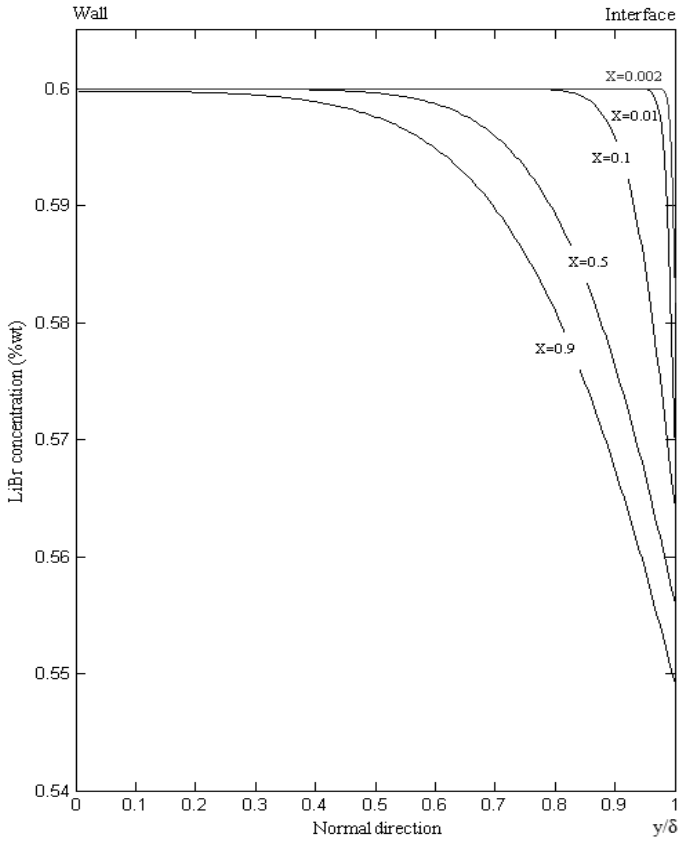

Figure 22. Cross stream LiBr concentration profiles at selected downstream positions, low temperature inlet (see Figure 9 for the definition of the domain)

The corresponding interface vapor absorption flux with distance around the tube is displayed in Figure 23. The rapid increase in the bulk temperature of the solution, as illustrated in Figures 19 and 21, leads to a significant decline in absorption efficiency as the solution travels around the tube, as seen in Figure 24. However, as the temperature profile evolves, allowing heat transfer from the film's surface to the cooling water (Figure 24), this decrease in absorption efficiency diminishes. Nevertheless, with the increase in surface vapor concentration, the driving force for absorption diminishes gradually, resulting in a gradual decrease in absorption rates as the solution circulates around the tube.

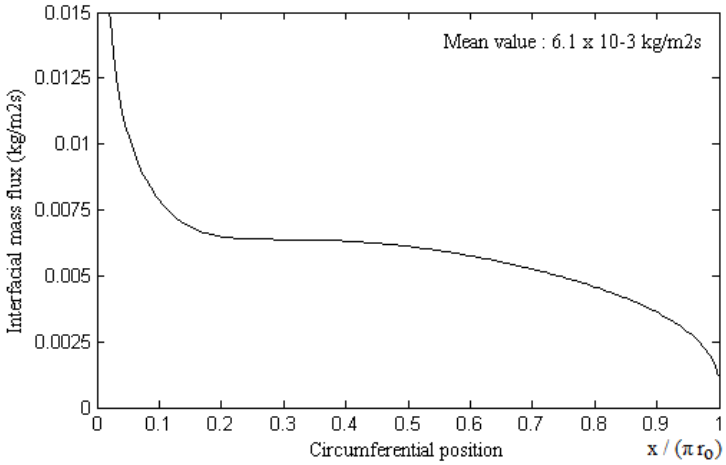

Figure 23. Variation of the interface vapour absorption flux with distance around the tube, low temperature inlet (see Figure 9 for the definition of the domain)

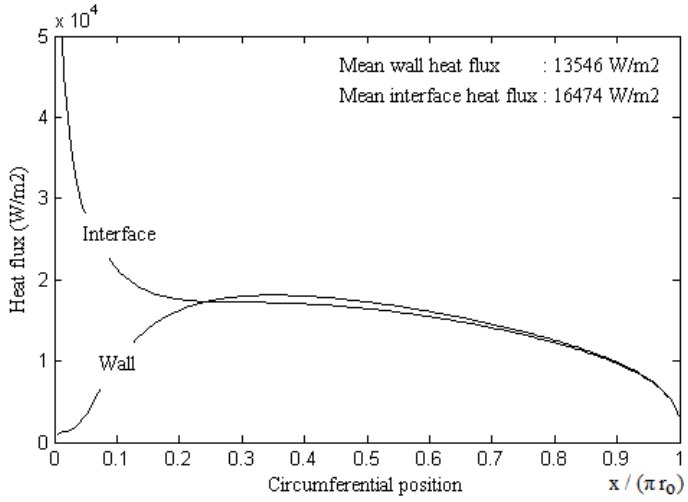

Figure 24. Variation of surface and wall heat flux with distance around the tube, low temperature inlet (see Figure 9 for the definition of the domain)

3.5. Effect of the Solution Inlet Temperature

The solution inlet temperature only effects the inlet region considerably. For the low solution inlet case, a large amount of absorption causes the bulk and surface vapour concentration to increase, hence driving potential for absorption decreases.

Figure 25 illustrates that, in scenarios where the solution enters at high temperatures, absorption rates increase as the temperature profile evolves, facilitating heat transfer from the surface to the wall. In most parts of the tube, both the bulk and surface vapor concentrations are lower compared to the scenario with a lower temperature solution inlet. Consequently, even though the low-temperature solution inlet condition initially has a considerable

advantage in the inlet region, the absorption rates in regions beyond the inlet for the high-temperature solution inlet condition are marginally higher than those in the low-temperature solution inlet condition. Nonetheless, the overall performance of the system with the low-temperature solution inlet is still about 6% higher.

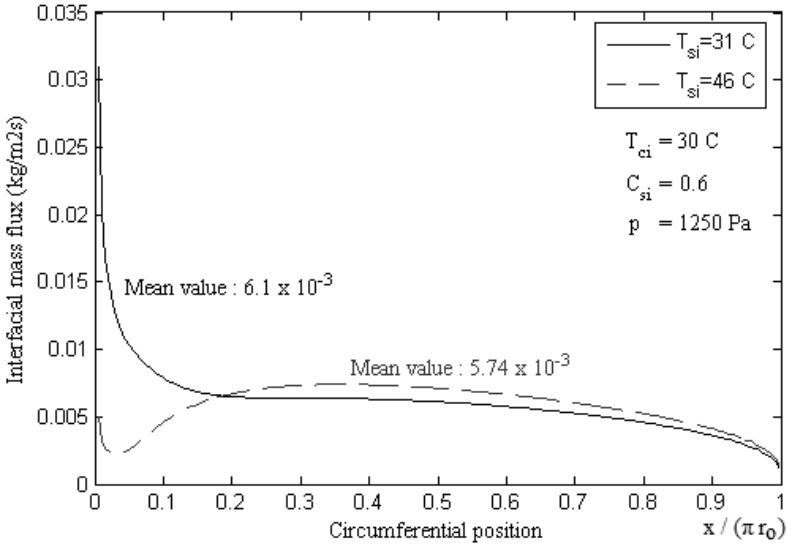

Figure 25. Surface vapour mass flux versus distance around the tube, effect of the solution inlet temperature (see Figure 9 for the definition of the domain)

3.6. Effect of the Solution Mass Flow Rate

Raising the mass flow rate of the solution leads to more resistance to heat transfer. Nevertheless, this results in a significant amount of absorption near the tube's entrance, reducing the absorption's driving potential as the solution continues through the tube. As shown in Figure 26, a higher mass flow rate correlates with diminished absorption efficiency. Specifically, increasing the Reynolds number from 5.38 to 10.77 results in a 2.5% drop in overall absorption efficiency. Further elevating the Reynolds number from 5.38 to 16.2 leads to a more pronounced decrease in absorption efficiency, totaling 5.26%.

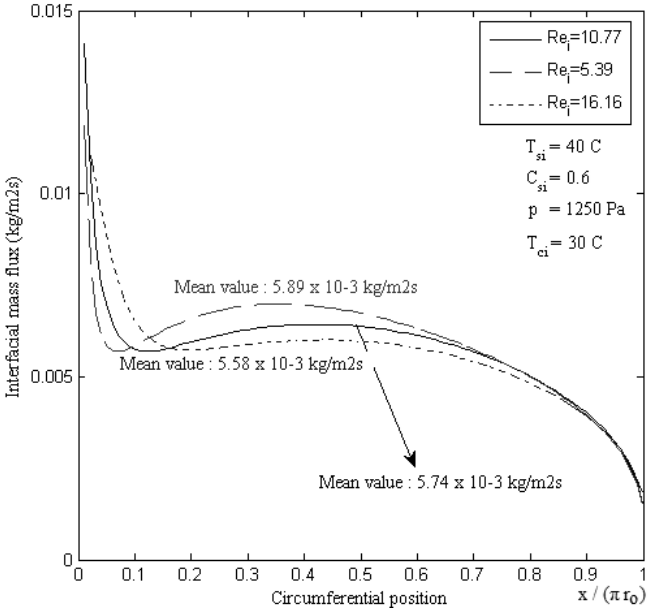

Figure 26. Surface vapour mass flux versus distance around the tube, effect of the solution mass flow rate (see Figure 9 for the definition of the domain)

3.7. Effect of the Cooling Water Inlet Temperature

The temperature of the cooling water significantly impacts absorption efficiency since vapor can only be absorbed if the heat generated during absorption is effectively transferred to the cooling water. Reducing the inlet temperature of the cooling water from 30°C to 25°C leads to a notable 26% enhancement in overall absorption performance, given the current parameters (as indicated in Figure 27). However, lowering the cooling water temperature in a cost-effective manner is often challenging, especially since it must remain above the ambient temperature when systems like cooling towers are used. In warmer regions, where the ambient temperature frequently exceeds 30°C, the cooling water's inlet temperature might reach as high as 35°C, which can significantly impair the performance of absorption systems.

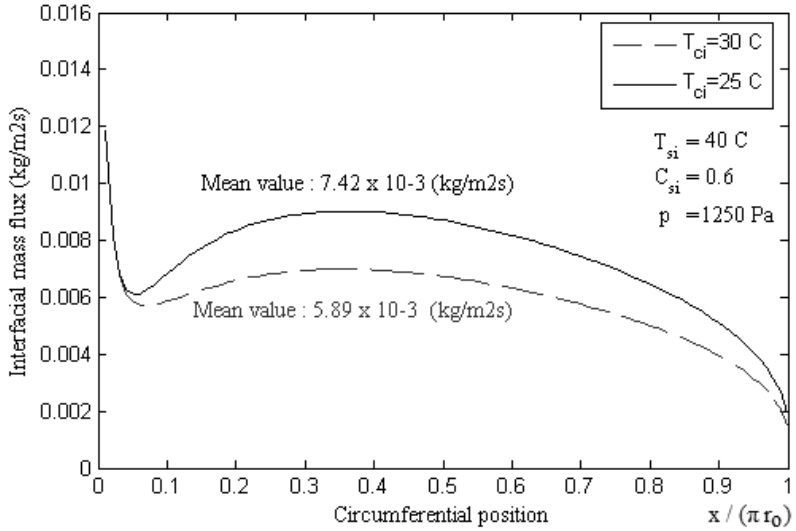

Figure 27. Surface vapour mass flux versus distance around the tube, effect of the cooling water inlet temperature (see Figure 9 for the definition of the domain)

4. Conclusions

This study provides an in-depth analysis of the performance of horizontal tubular absorbers in LiBr/H2O absorption refrigeration systems. Utilizing a computationally efficient two-dimensional model, validated against experimental data, we explored the impacts of key operational parameters, such as solution inlet temperature, mass flow rate, and cooling water inlet temperature, on absorption efficiency. Our findings emphasize the significant role of cooling water temperature, where a decrease in inlet temperature from 30°C to 25°C resulted in a notable 26% enhancement in absorption performance, underscoring the critical importance of thermal management. Additionally, while an increase in mass flow rate boosts initial absorption rates, it also raises heat transfer resistance, leading to a complex interplay that affects overall efficiency. Specifically, increasing the Reynolds number from 5.38 to 10.77 resulted in a 2.5% drop in overall absorption efficiency, and further elevating the Reynolds number to 16.2 led to a more pronounced decrease of 5.26%. Thus, optimal mass flow rates must balance these effects to maximize performance.

Moreover, lower solution inlet temperatures improve initial absorption due to higher driving forces for mass transfer, but this advantage diminishes downstream as the solution warms, suggesting the need for fine-tuning inlet conditions based on specific system requirements. Our findings emphasize the necessity of a multidimensional approach to the design and operation of absorption systems. By meticulously adjusting the cooling water temperature and solution mass flow rates, substantial improvements in system efficiency can be achieved.

Understanding the dynamic interplay between various parameters enables the development of more robust and adaptable absorption refrigeration solutions.

Future research should consider integrating advanced numerical models and real-time optimization techniques, such as artificial intelligence and machine learning, to enhance predictive capabilities and operational efficiency. Expanding the scope to include more complex hydrodynamic conditions and three-dimensional modeling will provide deeper insights into the absorber's performance under varied operational scenarios. This study offers valuable insights and practical guidelines for optimizing horizontal tubular absorbers, contributing to the advancement of efficient and sustainable absorption refrigeration technologies.

Acknowledgments

This publication is derived from a section of a Master's thesis entitled "Numerical analysis of absorbers used in LiBr/H2O absorption refrigeration." The thesis was presented to Dokuz Eylül University and examines absorbers in both vertical and horizontal flow configurations.

Author Statement

The authors confirm contribution to the paper as follows: study conception and design: Sercan Acarer; analysis and interpretation of results: Sercan Acarer, Nuri Kayansayan. All authors reviewed the results and approved the final version of the manuscript.

Conflict of Interest

The authors declare no conflict of interest.

References

Alcântara, S.C.S., Ochoa, A.A.V., Peixoto da Costa, J.Â., Duarte de Menezes, F. Leite, G.N.P., Michima, P.S.A., & Marques, A.S. (2023). Development of a Method for Predicting the Transient Behavior of an Absorption Chiller Using Artificial Intelligence Methods. *Applied Thermal Engineering*, 231, 120978.

Andberg, J. W., & Vliet, G. C. (1983). Nonisothermal Absorption of Gases into Liquid Films. *ASME-JSME Thermal Engineering Joint Conference Proceedings*, 2, 423-431.

Andberg, J. W. (1986). Absorption of Vapors into Liquid Films Falling Over Cooled Horizontal Tubes. *PhD Dissertation*, University of Texas, Austin.

Arroiabe, P.F., Martinez-Agirre, M. & Bou-Ali, M.M. (2022). Numerical Analysis of Different Mass Transfer Models for Falling Film Absorbers, *International Journal of Heat and Mass Transfer*, 182, 121892.

Asfand, F., Stiriba, Y. & Bourouis, M. (2016). Performance Evaluation of Membrane-Based Absorbers Employing H2O / (LiBr + LiI + LiNO3 + LiCl) and H2O / (LiNO3 + KNO3 + NaNO3) as Working Pairs in Absorption Cooling Systems, *Energy*, 115, 781-790.

Asfand, F., Stiriba, Y. & Bourouis. M. (2015). CFD Simulation to Investigate Heat and Mass Transfer Processes in a Membrane-Based Absorber for Water-LiBr Absorption Cooling Systems, *Energy*, 91, 517-530.

Castro, J., Farnós, J. Papakokkinos, G., Zheng, J. & Oliet, C. (2020). Transient Model for the Development of an Air-Cooled LiBr-H2O Absorption Chiller Based on Heat and Mass Transfer Empirical Correlations. *International Journal of Refrigeration*, 120, 406-419.

Florides, G. A., Kalogirou, S. A., Tassou, S. A., & Wrobel, L. C. (2003). Design and Construction of a LiBr–Water Absorption Machine. *Energy Conversion and Management*, 44, 2483–2508

Grigor'eva, N. I., & Nakoryakov, V. E. (1977). Exact Solution of Combined Heat and Mass Transfer Problems During Film Absorption. *Journal of Engineering Physics*, 33 (5), 1349-1353.

Hosseinnia, S.M., Naghashzadegan, M. & Kouhikamali, R. (2016). CFD Simulation of Adiabatic Water Vapor Absorption in Large Drops of Water–LiBr Solution, *Applied Thermal Engineering*, 102, 17-29.

Kakaç, S., & Liu, H. (1998). *Heat Exchangers: Selection, Rating and Thermal Design*. Boca Raton: CRC Press LLC.

Kwang, J. K. (1992). Heat and Mass Transfer Enhancement in Absorption Cooling. *PhD Dissertation*, Arizona State University.

Mortazavi, M., Isfahani, R.N., Bigham, S. & Moghaddam, S. (2015). Absorption Characteristics of Falling Film LiBr (Lithium Bromide) Solution Over a Finned Structure. *Energy*, 87, 270-278.

Papaefthimiou, V. D., Karampinos, D. C., & Rogdakis, E. D. (2006). A Detailed Analysis of Water-Vapour Absorption in LiBr-H_2O Solution on a Cooled Horizontal Tube. *Applied Thermal Engineering, 26*, 2095-2102.

Patankar, S. V. (1980). *Numerical Heat Transfer and Fluid Flow*. U.S.A.: Hemisphere Publishing Corporation.

Qu, M. (2008). Model Based Design and Performance Anaysis of Solar Absorption Cooling and Heating System. *PhD Dissertation*, Carnegie Mellon University.

Raisul Islam, M., Wijeysundera, N. E., & Ho, J. C. (2006). Heat and Mass Transfer Effectiveness and Correlations for Counter-Flow Absorbers. *International Journal of Heat and Mass Transfer*, 49, 4171-4182.

Seol, S. S., & Lee, S. Y. (2005). Experimental Study of Film Flow and Heat/Mass Transfer in LiBr–H2O Solution Flowing Over a Cooled Horizontal Tube. *International Communications in Heat and Mass Transfer, 32*, 445-453.

Sui, Z., Sui, Y. & Wu, W. (2022b). Multi-Objective Optimization of a Microchannel Membrane-Based Absorber with Inclined Grooves Based on CFD and Machine Learning, *Energy*, 240, 122809.

Sui, Z., Zhai, C. & Wu, W. (2022a). Parametric and Comparative Study on Enhanced Microchannel Membrane-Based Absorber Structures for Compact Absorption Refrigeration. *Renewable Energy*, 187, 109-122.

Tsai, B., & Perez-Blanco, H. (1998). Limits of Mass Transfer Enhancement in Lithium Bromide-Water Absorbers by Active Techniques. *International Journal of Heat and Mass Transfer*, 41 (15), 2409-2416.

Wen, T., Lu, L. & Luo, Y. (2021). Review on the Fundamentals and Investigations of Falling Film Dehumidification/Absorption Refrigeration Based on CFD Technology. *International Journal of Heat and Mass Transfer*, 171, 121042.